Nanotribology of Ionic Liquids: Transition to Yielding Response in Nanometric Confinement with Metallic Surfaces

Antoine Lainé, Antoine Nigues, Lydéric Bocquet, Alessandro Siria

Nanotribology of Ionic Liquids: Transition to Yielding Response in Nanometric Confinement with Metallic Surfaces

Antoine Lainé, Antoine Niguès, Lydéric Bocquet, and Alessandro Siria*

Laboratoire de Physique de l'École Normale Supérieure, ENS, Université PSL, CNRS, Sorbonne Université, Université Paris-Diderot, Sorbonne Paris Cité, UMR CNRS 8550, 24 Rue Lhomond 75005 Paris, France

(Received 8 November 2019; revised manuscript received 20 January 2020; accepted 10 February 2020; published 20 March 2020)

Room-temperature ionic liquids (RTILs) are molten salts which exhibit unique physical and chemical properties, commonly harnessed for lubrication and energy applications. The pure ionic nature of RTIL leads to strong electrostatic interactions among the liquid, furthermore exalted in the presence of interfaces and confinement. In this work, we use a tuning-fork-based dynamic surface force tribometer, which allows probing both the rheological and the tribological properties of RTIL films confined between a millimetric sphere and a surface, over a wide range of confinements. When the RTIL is confined between metallic surfaces, we see evidence of an abrupt change of its rheological properties below a threshold confinement. This is reminiscent of a recently reported confinement-induced capillary freezing, here observed with a wide contact area. In parallel, we probe the tribological response of the film under imposed nanometric shear deformation and unveil a yielding behavior of the interfacial solid phase below this threshold confinement. This is characterized by a transition from an elastic to a plastic regime, exhibiting striking similarities with the response of glassy materials. This transition to yielding of the RTIL in metallic confinement leads overall to a reduction in friction and offers a self-healing protection of the surfaces avoiding direct contact, with obvious applications in tribology.

DOI: 10.1103/PhysRevX.10.011068

Subject Areas: Materials Science, Nanophysics, Soft Matter

I. INTRODUCTION

Room-temperature ionic liquids (RTILs) are intriguing materials: They exhibit standard features of liquid matter, but their molten salt nature, associated with the strong Coulombic interaction between molecules, is quite unique and leads to a variety of specific properties which are harnessed in numerous applications from electrochemistry to tribology. Their behavior usually challenges well-established frameworks inherited from liquid state theory or that of dilute electrolytes [1–3]. This unique response is furthermore exalted under confinement or at interfaces, and a rich variety of behaviors have been observed for RTILs under confinement [4–8], with a strong dependence on the nature of the interfaces [9–12]. Experimentally, atomic force microscopy (AFM) [13] is a technique of choice to probe the properties of RTIL in confinement, as well as the surface force apparatus [14,15]. A notable difference between the two approaches is the lateral size of the probed contact, which ranges from tens of nanometers for AFM to microns in the surface force apparatus. Also, properties are mostly investigated with insulating confining surfaces, but recent work has put forward the specificity of metallic confinement for RTILs, with the evidence of a confinement-induced capillary freezing resulting associated with the metallic nature of the surfaces [16]. That the nature of electric boundary conditions may affect the properties of charged molten salt is actually quite expected [17]. However, the impact of metallic confinement on the properties of confined RTILs remains to be fully assessed and calls for new experimental investigations. Furthermore, metallic surfaces are ubiquitous in applications of RTILs, e.g., for lubrication, where RTILs are expected to be excellent boundary lubricants [18,19], as well as in electrochemistry [20]. In the present work, we use a newly introduced force measurement methodology, based on a macroscopic tuning fork [21,22] and here combined with electric measurements, in order to probe the equilibrium and out-of-equilibrium frictional properties of RTILs confined between extended metallic surfaces. This instrument allows us to probe both the rheology of the confined materials, as well as its tribological properties under shear. As in Ref. [16], the ionic liquid under scrutiny is

*alessandro.siria@lps.ens.fr

$BmimBF_4$, exhibiting a viscosity $\eta \approx 50$–130 mPa s at room temperature [23] and a bulk freezing temperature $T_B \approx -71\,°C$ [16] (See Appendix, Sec. I).

II. EXPERIMENTAL SETUP AND MATERIALS

A gold-coated sphere of nanometric roughness (see Appendix, Sec. II, Fig. 5) and radius $R \sim 1.5$ mm is glued on one prong of a centimetric aluminium tuning fork [Fig. 1(a)] used as a force sensor. A piezodither mechanically excites the tuning fork and an accelerometer monitors the oscillation amplitude and phase shift along the normal (blue) and shear (red) directions. In the following we will refer to the *normal probe* as the nanorheology probe since it provides information on the viscoelastic properties of the confined fluid; conversely, we will refer to the *shear mode* as the nanotribology probe since it provides information on the mechanical shear response under an imposed excitation. The present instrument allows probing the two modes simultaneously.

A piezoscanner imposes the confinement distance D over several micrometers with subnanometer precision. The two polarizable surfaces enable us to impose a voltage difference ΔV and record the electric current flowing through the contact [Fig. 1(b)] with an I/V amplifier. To prevent the contamination of RTILs from ambient humidity and possible modification of the mechanical properties of nanoconfined RTILs [24], the entire setup is kept in a vacuum chamber with the pressure below 10^{-1} mbar. The centimetric tuning fork serves as force sensor and enables simultaneous normal and shear measurements by exciting two orthogonal modes of the tuning fork [22], both presenting a high stiffness $K \sim 10^5$–10^6 N/m and a high quality factor $Q_0 \sim 10^3$. The oscillation amplitude range lies from 200 nm down to 2 nm. As in standard frequency modulation AFM [21] a conservative interaction leads to a

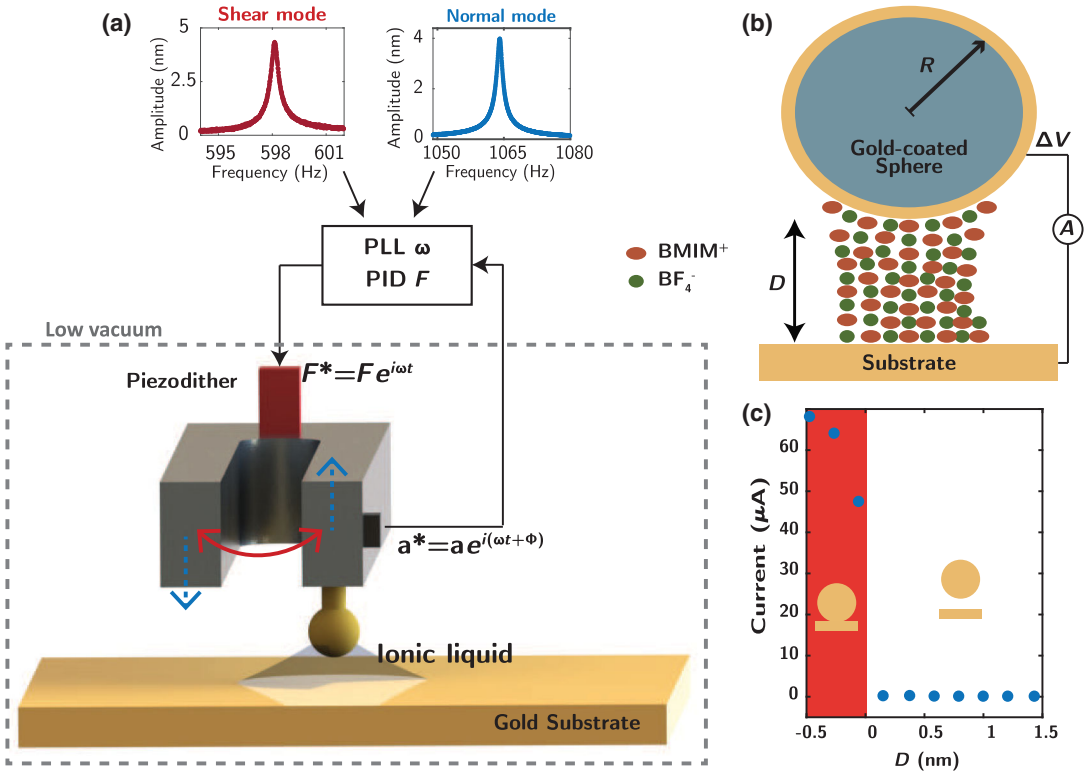

FIG. 1. Experimental setup. (a) Schematic representation of the force measurement apparatus. The prongs of the tuning fork oscillate along a shear (red) and a normal (blue) mode simultaneously. The two curves at the top show the corresponding resonance curves. The mechanical excitation $F^* = Fe^{i\omega t}$ $[N]$ is induced by the actuation of an external piezodither. An accelerometer glued on one prong records the dynamic oscillation amplitude $a^* = ae^{(i\omega t+\phi)}$ $[m]$. A lock-in amplifier extracts the amplitude and phase of the accelerometer signal. The phase difference is continuously kept at zero by use of a phase-locked loop (PLL) which varies the excitation frequency (ω) accordingly. A feedback loop (PID) controls the excitation intensity F in order to keep the oscillation amplitude a chosen value. A spherical probe, glued at the end of one prong, is immersed in an ionic liquid drop deposited on a gold substrate. The setup is placed in a reduced pressure ($P < 10^{-1}$ mbar) environment. (b) The ionic liquid $BmimBF_4$ is confined between the substrate and the gold-coated sphere of radius $R \approx 1.5$ mm. A piezoscanner varies the confinement distance D over tens of micrometers with subnanometric precision. A potential difference $\Delta V \approx 25$ mV is applied between the polarizable surfaces. (c) Electric current flowing through the contact upon decreasing the separation distance D.

shift of the oscillator resonance frequency $f_0 \to f_0 + \delta f$ and a dissipative force implies an extra damping which broadens the resonance $Q_0 \to Q_0 - \delta Q$. Despite the size of the force probe, this experimental setup was already shown to display the force sensitivity required for atomic force microscopy [21] and even detection of subnanometric layering of RTILs confined between a (insulating) mica surface and glass bead [22].

A voltage difference of $\Delta V \approx 25$ mV is furthermore applied between the gold surface and the gold-coated sphere [Fig. 1(b)]. This allows us to determine the absolute zero separation distance from the electric-current response [Fig. 1(c)]. Indeed, the electronic conductivity of RTILs is negligible [8], so that the strong increase of the current as observed in Fig. 1(c) is the signature of the direct contact between the gold surface with the gold-coated sphere. The value of the applied voltage difference is chosen far below the RTILs electrochemical window. We observe from the results shown in the Appendix, Sec. V, Fig. 8, that this value does not qualitatively influence the results.

III. NANORHEOLOGY MEASUREMENTS

Figure 2 presents the simultaneous measurement of the normal and tangential impedance as the separation distance is decreased from micrometers down to direct contact between the confining metallic surfaces (see [22] for more details about the computation of the mechanical impedance). The separation distance corresponds to a mean value around which the probe oscillates with an amplitude given by the normal oscillation amplitude. The important stiffness of the entire setup enables us to fully squeeze out the confined liquid until direct surfaces contact is reached. The normal oscillation of the sphere creates a squeeze flow with typical extension $\sim\sqrt{2RD}$ [25]. The associated dissipative normal impedance due to the liquid viscosity thus reads

$$Z_N'' = \frac{6\pi\eta R^2 \omega_N}{D - D_0}, \tag{1}$$

where R is the sphere radius, $\omega_N = 2\pi f_N$ the normal oscillation frequency, η the fluid viscosity, and D_0 the position of the no-slip plane, usually called hydrodynamic zero. The linear behavior of the inverse of the normal damping impedance $1/Z_N''$ with respect to separation distance D [Fig. 2(a)] shows evidence of the liquidlike rheological response down to hundreds of nanometers. The linear fit (dashed blue line) provides a viscosity $\eta \approx 60$ mPa s comparable with previous measurements [23]. Besides, the long-range viscous response allows for a determination of the flow boundary condition and provides a hydrodynamic zero $D_0 \approx 10$ nm with respect to the contact defined by electrical measurements. Assuming that the strong electrostatic interactions between ions and the metallic surfaces prevent any slip at the interface, such nonzero D_0 means that some solid prewetting films are not fully mobilized by the oscillatory squeeze flow. Such interfacial nanostructure of a few nanometers were observed *in situ* by atomic force microscopy [16] as well as scanning tunneling microscopy [26]. Here, long-range hydrodynamic flow measurement, with a hydrodynamic probe of effective radius $\sqrt{2RD} \approx 50$ μm, accurately resolves the nanometric interfacial features.

IV. FRICTIONAL RESPONSE

Simultaneous shear measurements show evidence that the shear mechanical impedance Z_S^* of the bulk RTILs remains negligibly small until nanoconfinement is reached [Fig. 2(b)]. For separation distance ≈50 nm we observe an important increase of both the elastic (black) and dissipative (red) shear modulus. Further decreasing the separation distance D (blue zone), the shear impedance

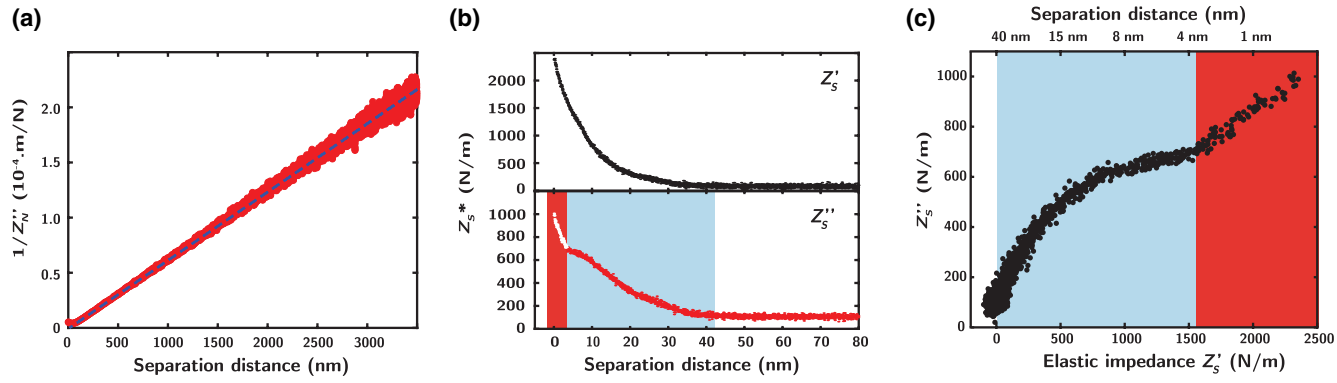

FIG. 2. Nanorheological and nanotribological measurements. (a) Inverse of the normal dissipative impedance $1/Z_N''$ as a function of separation between the surfaces. The dashed line results from a linear fit characteristic of viscous damping. The normal oscillation amplitude is $a_N \sim 2$ nm. (b) Evolution of the conservative Z_S' (black) and dissipative Z_S'' (red) shear impedance as the separation distance is varied. A solidlike mechanical behavior of the nanoconfined RTILs is observed from ~40-nm confinement (blue zone) down to the direct metallic contact (red zone and white data points). The shear oscillation amplitude is $a_S \sim 3$ nm. (c) Corresponding shear dissipative impedance Z_S'' as a function of shear elastic impedance Z_S' highlighting an abrupt change of frictional behavior.

keeps increasing, as well as the imposed shear strain $\gamma = a_S/D$ and the indentation contact area $\mathcal{A}_{\text{eff}}$, until direct metallic contact is reached (red zone). As we indent into the interfacial phase (blue zone), the elastic response strongly dominates while the dissipative part tends to saturate around $Z_S'' \approx 0.7$ kN/m corresponding to a dissipation $F_S \approx 2.5$ μN. An important conclusion from this measurement is that the predominance of the elastic part highlights the solidlike behavior of the interfacial film, along with the limited frictional dissipation. We emphasize that in the case of standard silicon oil, no such response is obtained (see Appendix, Sec. III, Fig. 6). Also, an important remark is that this behavior is not observed for the RTIL confined between insulating surfaces (see Appendix, Sec. IV, Fig. 7). Here, this behavior was observed for several approach-retracts at the same and at different locations on the substrate. We report the observation of this shear mechanical response at an average distance $\lambda_S \approx 60$ nm from the electric contact, and independent on the tangential and normal oscillation amplitude. We note that the measurement of a critical confinement below which a solidlike behavior is observed is in agreement with the previous report in Ref. [16], although with a probe radius around 3 orders of magnitude bigger.

Considering the frictional properties of the RTILs, we plot the evolution of Z_S'' as a function of Z_S' [Fig. 2(c)] and we observe a decrease of the slope while dissipating in the solidlike structure (blue zone); then, above a threshold associated with an elastic interaction $Z_S' \approx 1$ kN/m, the dissipative impedance tends to saturate with increasing elastic impedance. Finally, for a separation distance under 4 nm, we observe an abrupt change of behavior and a strong increase of the dissipation (red zone). As the load increases with decreasing D, the abovementioned slope can be qualitatively related to a friction coefficient. Thus, the solidlike nature of the interfacial film of RTIL not only protects the metallic surfaces from direct contact, but, moreover, enables us to lubricate the contact by reducing the frictional dissipation in the saturated region (where this effective friction coefficient is substantially reduced, see below).

V. SHEAR MECHANICAL PROPERTIES

While we first concentrated on the normal response and the resulting nanorheology properties, we now turn to the investigation of the response of the confined film under shear. This allows us to characterize the frictional properties of the interfacial material under shear by varying the imposed lateral oscillation amplitude.

We plot in Fig. 3(a) the shear mechanical properties of the interfacial solid phase as a function of applied shear strain $\gamma = a_S/D$. In this figure, the confinement is fixed to $D = 10$ nm. We observe a shear softening of the interfacial structure (order of magnitude estimate discards any thermally induced material softening, see Appendix, Sec. VI) and the elastic and dissipative response do cross above a threshold strain γ_Y. Such a signature is usually associated with the yielding nature of the investigated material [27]. The characteristic yield point—vertical dashed line—separates an elastic regime at low shear strain and a plastic, dissipation-dominated, regime at high shear strain [Fig. 3(a)].

The transition from elastic to plastic mechanical response is also observed from the different stress-strain curves [Figs. 3(b) and 3(c)] where the shear stress is defined here as $\sigma = Z_S'' a_S/\mathcal{A}_{\text{eff}}$ with $\mathcal{A}_{\text{eff}}$ the effective contact area. The solid nature of the interfacial film makes the classical Hertz model of contact mechanics suitable to derive an estimate for the effective contact area. Therefore, we use from now the approximation $\mathcal{A}_{\text{eff}} \approx \mathcal{A}_{\text{Hertz}}$ where $\mathcal{A}_{\text{Hertz}} = 2\pi R\delta$, with the indentation depth $\delta = \lambda_S - D$ (see the discussion on contact effective area in the Appendix, Sec. VII).

We plot in Fig. 3(b) the stress versus strain curve for two different imposed shear amplitude a_S. For a small shear amplitude, $a_S = 6$ nm (top panel), we observe first a linear regime where $\sigma = \sigma_Y + G''\gamma$ before reaching a peak stress

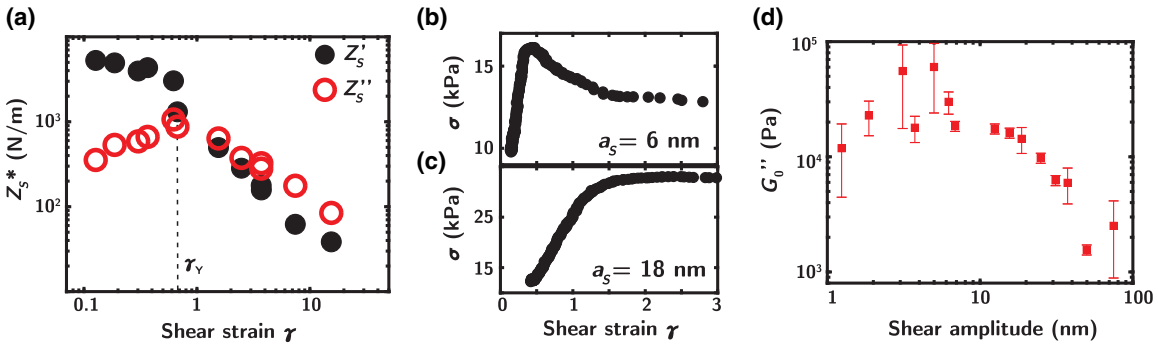

FIG. 3. Shear mechanical properties of the solid interfacial phase. (a) Shear mechanical impedance Z_S^* as a function of applied shear strain for a fixed confinement distance $D = 10$ nm. (b),(c) Stress-strain curves at constant shear amplitude $a_S = 6$ nm and $a_S = 18$ nm, respectively. (d) Dissipative shear modulus G'' as a function of shear amplitude obtained from fitting the linear part of the different stress-strain curves. Error bars represent the standard error.

and eventually a plateau at larger strain. Now, increasing the shear amplitude to $a_S = 18$ nm (bottom panel), the stress overshoot disappears and the linear regime is directly followed by a plateau. This qualitative behavior change as well as the shear dissipative modulus decrease with increasing amplitude [Fig. 3(d)] is reminiscent of the existence of a critical yield point above which the material gets fluidized. Let us now analyze more in detail the various elastic and plastic regimes.

A. Elastic regime

In the elastic regime $\gamma < \gamma_Y$, the conservative mechanical impedance is fairly constant and strongly dominates the dissipative part by one order of magnitude [Fig. 3(a)]. The imposed shear deformation remains relatively small and the interfacial phase elastically compensates the deformation. From this initial plateau, and using a Hertz contact mechanics model to approximate the contact area $\mathcal{A}_{\text{eff}} \approx \mathcal{A}_{\text{Hertz}} = 2\pi R(\lambda_S - D) \approx 400\ \mu\text{m}^2$, we obtain an estimate of the elastic shear modulus $G_0' \approx (D/\mathcal{A}_{\text{eff}})Z_{S0}' \approx 130$ kPa. Interestingly, the dissipative shear modulus for small shear amplitude lies around $G_0'' \approx 20$ kPa [Fig. 3(d)] and is therefore one order of magnitude smaller than G_0'. Using the following formula $E_0' = 2G_0'(1+\nu)$, valid for isotropic material, and arbitrarily assuming a Poisson ratio $\nu = 0.2$ provides a rough estimate of the Young modulus $E_0' \approx 300$ kPa. This value is only a crude estimate as the interfacial film is very likely not to be isotropic and the Poisson ratio is externally imposed.

B. Yielding and plastic regime

By increasing the shear strain above the yield strain $\gamma > \gamma_Y$, we observe on Fig. 3(a) a transition from an elastic to a plastic regime, where the dissipation overcomes the elastic response of the system. Such behavior is reminiscent of the yielding mechanism observed in emulsions and glassy materials [27,28]. At the yield point, the elastic impedance sharply decreases and the dissipative impedance reaches its maximum value. From Fig. 3(a) we can extract a value of the yield force F_Y, the maximum applied force the system is capable to handle elastically, from the relation $F_Y = Z_Y'\gamma_Y D$ where Z_Y' is the elastic impedance and γ_Y the shear strain, both at the yield point. We extract the values $Z_Y' \approx 3000$ N/m and $\gamma_Y \approx 0.7$, eventually giving an experimental value of the yield force $F_Y \approx 2.1\ \mu$N and a corresponding yield strength $\sigma_Y = F_Y/\mathcal{A}_{\text{eff}} \approx 5$ kPa. From fitting the linear part of the stress-strain curves, we estimate $\sigma_Y \approx 4$ kPa in excellent agreement with the first estimate. This value is about 1 to 2 orders of magnitude smaller than the estimated Young modulus E_0'. This is typical of a defect-mediated yielding mechanism [29] and points toward an amorphous or polycrystalline structure of the interfacial film.

For shear strain above γ_Y, the response of the system is dominated by the dissipation. Both the elastic and dissipative parts of the impedance decrease with increasing shear, thus eventually pointing toward a shear induced fluidization of the interfacial structure. The disappearance of the peak stress under an increase of the shear amplitude [Fig. 3(c)] further corresponds to the mechanical response of an amorphous solid [30]. The stress overshoot, possibly resulting from a delayed activation, disappears in the fluidized plastic regime because the activation barrier is more easily crossed.

VI. TRANSITION TO GLASSY RESPONSE IN CONFINEMENT

The observed mechanical behavior highlights strong similarities with the mechanical response of glassy materials. In the theoretical interpretation developed in a previous study [16,17], it was argued that the RTIL undergoes a capillary freezing in confinement: The shift of the crystallization temperature results from the stabilization of the solid phase due an image charge effect at the metallic surfaces. However, the properties of the highly confined material could not be investigated previously: Here, using the new instrument, we show that the transition to the solid state under confinement does not reach a state with crystalline response, but rather exhibit the properties of a yielding, glassylike state. Such a frustrated transition is to be expected due to kinetic barriers. This is further supported by observations from the literature. Indeed, bulk differential scanning calorimetry measurements report that RTILs get supercooled and form glasses rather than crystallize [31]. Besides, 2D IR spectroscopy of RTILs thin films also presents a dynamical molecular behavior that fully resembles the one of a supercooled liquid [32]. The mechanical measurements performed on solidlike, fully crystallized, interfacial systems obtained from drop casting of RTILs-methanol solution provides a measure of the Young modulus $E^* \approx 60$ MPa [33]. Here, we obtain a value that is about 2 orders of magnitude smaller and further points toward the glassy nature of the nanoconfined RTILs.

VII. SHEAR DISSIPATION-VELOCITY DEPENDENCE

The dependence of the shear dissipation force F_D on the shear velocity v provides further insight into the mechanisms governing the dissipative response of the interfacial glassy structure.

As we show In Fig. 4(a), for a fixed separation distance $D = 25$ nm, we observe a logarithmic dependence of F_D with respect to the shear amplitude a_S. Such response is actually expected for glassy materials undergoing plastic reorganization. In the framework of a Eyring's theory, commonly used to describe the mechanical response of

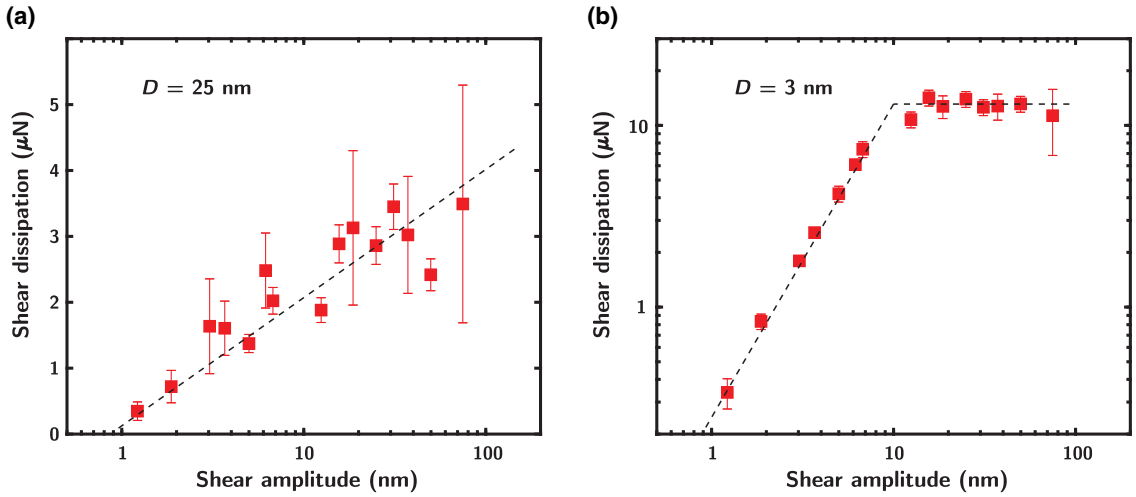

FIG. 4. Shear frictional properties of the solid interfacial phase. (a) Logarithmic dependence of the dissipative friction force with respect to the shear amplitude for a fixed confinement distance $D = 25$ nm. (b) Transition from a power-law to solid friction for fixed separation distance $D = 3$ nm. Error bars represent the standard error and correspond to 10% for single points.

glassy materials in terms of a shear induced activation process [34], the shear stress reads

$$\sigma_D = F_D/\mathcal{A}_{\text{eff}} = \frac{k_B T}{V^*} \ln\left(\frac{a_S}{a_{S0}^*}\right),$$

where V^* the activation volume corresponds to the elementary volume over which a plastic event occurs. From the fit of the data, we obtain a typical size for the activation volume $l^* \sim (V^*)^{1/3} \approx 10$ nm. Altogether, this emphasizes the glassy behavior of the interfacial layer where the dissipation is triggered by plastic events taking place on a length scale of several nanometers. In this regime, the dissipative events are to occur at the weaker points in the system and these ones are more likely to appear in the bulk than in the close vicinity of the interface where short-range wetting structures are present and strongly pinned to the surface.

Further decreasing the confinement distance down to $D = 3$ nm [Fig. 4(b)], we observe striking differences in the frictional response. The shear dissipation to amplitude curve exhibits a power-law behavior $F_D \sim a_S^\alpha$ at low amplitude with an exponent $\alpha \approx 1.5$, whereas for higher amplitude, above $a_c \approx 10$ nm, solidlike friction is observed with a constant dissipative force. Confinement in the latter case is below the characteristic length scale of plasticity, $l^* \approx 10$ nm, obtained above from the elementary activation volume $l^* \sim V^{*1/3}$. Accordingly, the different signature of the shear force highlights a change of regime where one probes dissipation below the elementary length scales associated with plastic events. This is furthermore consistent with the observation that the transition from the regime in Figs. 4(a) to 4(b) appears smoothly around $D \sim$ 10–15 nm (not shown). For such small separation distance, the roughness of the confinement surfaces may also influence the frictional response of the nanoconfined RTIL.

VIII. CONCLUSION

In this work, we have exploited the capabilities of a recently introduced tuning-fork-based dynamic surface force instrument, which allows us to perform a joint investigation of nanorheology and nanotribology of confined films with a millimetric probe down to nanoscale confinements. This instrument effectively bridges the gap between atomic force probes and large scale tribology and hence provides an exhaustive overview of the mechanical response of the investigated material in confinement.

We show that a room-temperature ionic liquid confined between *metallic surfaces* exhibits a transition toward solidlike mechanical response below a threshold confinement. This observation agrees with a previous report [16], however, highlighted here with a millimetric probe and wide contact area. Furthermore, the joint nanorheology-tribology approach allowed by our instrument shows that the ionic liquid undergoes a transition toward a glassy state, with a yielding behavior above a threshold shear strain. Previous theoretical work interpreted the change of mechanical response of the ionic liquid as a freezing transition [16,17] occurring in metallic confinement due to image charge effects. However, the present work demonstrates that the materials do not exhibit the response of fully crystalline materials, but rather the yielding response of glassy materials. Accordingly this indicates that the predicted freezing transition in confinement is either incomplete (leading to a polycrystalline structure) or frustrated (leading to an amorphous structure). One route to enhance the liquid-to-solid transition would be to use a specific cation-anion pair more likely to freeze, for example, like the ion pair used in [35] where a liquid-to-solid transition is reported under confinement. Even if the underlying mechanism is different from the results reported

here (the interfacial structure remains solid even for micrometer separation distance), the final output could be to increase even more the stability of the solid phase. With the increasing appeal to use RTIL as an electrolyte in the supercapacitor, our results indicate that some care should be taken while designing such devices involving an important interfacial contact between RTILs and metallic surfaces since the simple picture of a fully liquid electrolyte may not be valid anymore. Such RTILs freezing under confinement could imply a nonuniform *a priori* lowered ionic mobility in the porous matrix and eventually impact the system's power capabilities. Because of the inherent geometric difference between the nanoslit where confinement is restricted to one dimension and the pore of an electrode with three-dimensional confinement, a direct mapping of our results to the case of a porous matrix is not straightforward. More importantly, our observations points to key applications in tribology. Indeed, the confinement-induced transition of the ionic liquid transforms the liquid into a solidlike film which acts as a good lubricating layer and reduces frictional dissipation. The interfacial solid phase is self-consistently generated under confinement between metallic surfaces and therefore acts as a "sacrificial" antiwear film, protecting the surfaces from direct contact. Such characteristics, in addition to manifold appealing physical properties of RTILs (low vapor pressure, high thermal stability, and wide electrochemical window), makes them ideal candidates as antiwear boundary lubricants [36]. We emphasize that the response reported here is observed under vacuum conditions and the presence of water in RTILs may screen the electrostatic interactions at stake and then reduce or even mask the mechanical properties highlighted here. Then it may prove to be important to prefer hydrophobic RTILs in order to take full advantage of such a mechanical response. Furthermore, future work may also explore the capabilities of RTILs as *active lubricant*, via the control of interfacial properties thanks to surface electric polarization [18,37–39]. This will open new routes for unforeseen lubricating mechanisms.

ACKNOWLEDGMENTS

A. S. acknowledges funding from the European Union's Horizon 2020 Framework Program/European Research Council Starting Grant No. 637748 NanoSOFT. L. B. acknowledges support from the European Union's Horizon 2020 Framework Program/European Research Council Advanced Grant No. 785911 Shadoks.

APPENDIX: MATERIALS AND CONTROL EXPERIMENTS

1. Ionic liquid description

The ionic liquid used is BmimBF4 and presents a typical ion pair size $l \approx 0.8$ nm. This liquid exhibits a viscosity around 100 mPa s at room temperature [23] and a bulk freezing temperature $T_B = -71\,°\mathrm{C}$ [16]. The liquid is constantly stored in a separate vacuum chamber. Right before use, it is filtered in a 20-nm pore membrane. Once installed in the vacuum chamber where the experiments are performed, the IL is left around 12 h prior to performing any measurement. The reduced pressure environment prevents the contamination from ambient humidity, as evidence has been shown that the mechanical properties of nanoconfined RTILs depend on the environmental humidity [24].

2. AFM images of the surfaces

Metal deposition via evaporation is performed in a clean room to obtain the gold-coated confinement surfaces. The probe is a smooth glass sphere and the substrate an undoped silicon wafer. For both surfaces, a 5-nm adhesive Cr layer is deposited and then a 150-nm-thick gold layer is added to obtain good metallic properties. AFM images of the surfaces are shown in Fig. 5.

3. Comparison with silicon oil

In order to benchmark our apparatus, we first perform measurements with silicon oil and observe a slight frictional response below 20 nm from the surface.

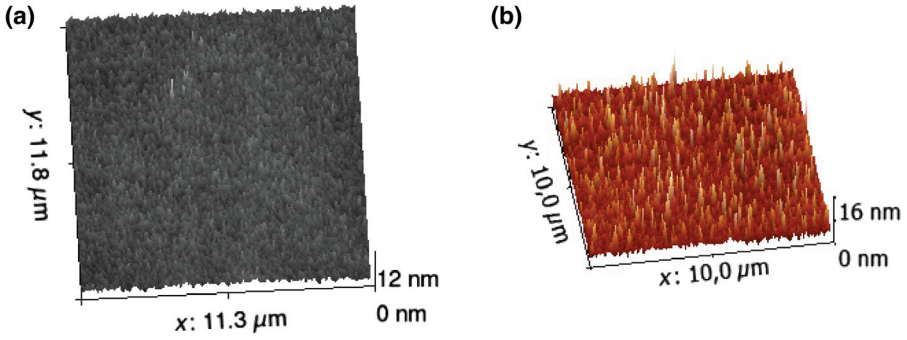

FIG. 5. AFM image of (a) the gold substrate (rms roughness ≈0.9 nm) and (b) the gold-coated sphere (rms roughness ≈1.5 nm). For the sphere, the spherical background of the raw AFM image is substracted.

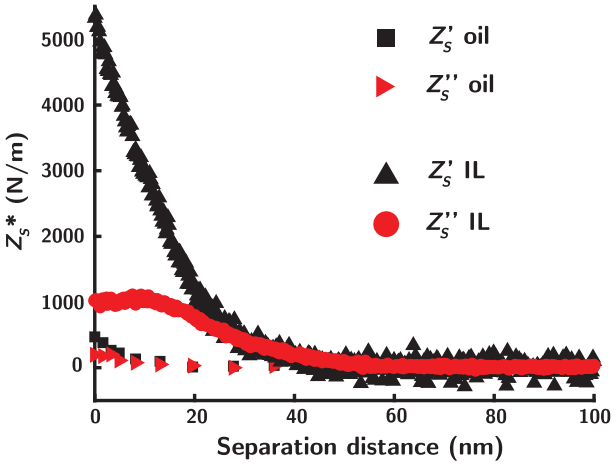

FIG. 6. Shear impedance measurement for ionic liquid (IL) and silicon oil. The shear oscillation amplitude is 6 nm for both measurements.

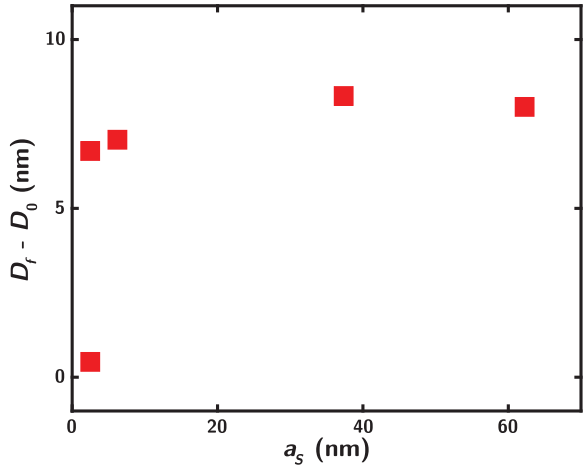

FIG. 7. Comparison of the hydrodynamic zero D_0 and the position of the frictional response D_f as a function of the applied shear oscillation amplitude a_S for insulating confinement surfaces.

Then at the same oscillation amplitude, the RTIL exhibit a frictional response orders of magnitude bigger a frictional response orders of magnitude bigger as shown in Fig. 6.

4. Measurement with insulating surfaces

We perform measurements with a glass sphere without any metallic coating on the surface and a freshly cleaved mica surface. Such insulating surfaces forbid any current measurement flowing through the contact and therefore we only compare the hydrodynamic zero D_0 with the position of the frictional contact D_f. We observe in Fig. 7 that the frictional zero appears only some nanometers before the hydrodynamic one. Then no solidlike structure is observed with insulating surfaces and the RTIL remains liquid down to ultimate confinement.

5. Impact of the voltage difference on the frictional behavior

In order to check that the imposed voltage does not significatively influence the mechanical response of the nanoconfined RTILs, we perform shear force measurements with different applied voltage difference. The shear mechanical impedance of three consecutive measurements is shown in Fig. 8. By increasing the potential difference from $\Delta V = 100$ mV up to $\Delta V = 600$ mV, we observe qualitatively a similar behavior. Focusing on the elastic impedance, in Fig. 8(a), we observe a slight increase of Z_S' at a very small distance with increasing the voltage difference but the shape of the response remains the same. We observe in Fig. 8(b) a similar behavior for the dissipative impedance in the three cases within the resolution of our instrument.

6. Local interfacial structure heating

The fluidization could be induced by a local heating due to the dissipated power induced by the probe oscillation. We estimate this local heating by balancing the power dissipated by the probe oscillation $P_{\mathrm{osc}} = Z_S'' a_S^2 \omega$

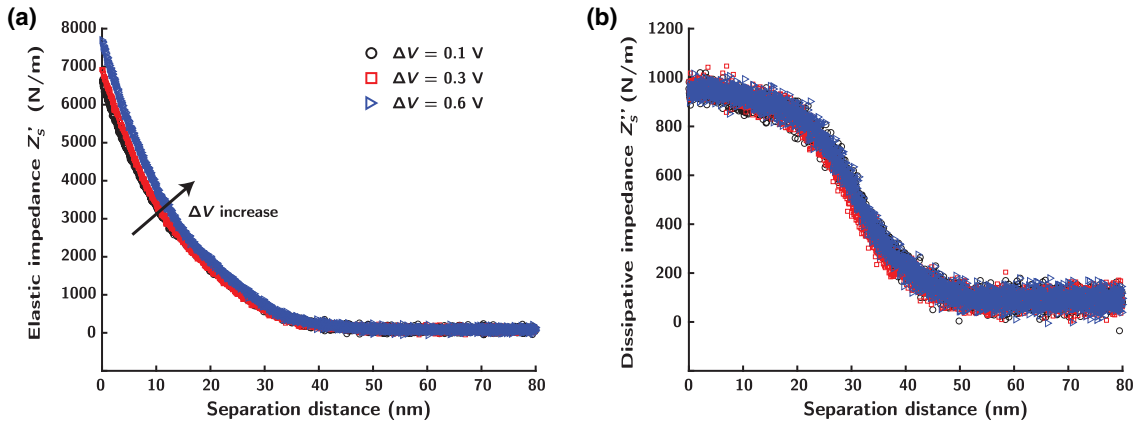

FIG. 8. Shear impedance measurement with different applied voltage difference. Shear amplitude is 5 nm.

and the induced thermal power $P_{\mathrm{th}} = \mathcal{A}_{\mathrm{eff}}\lambda\Delta T/D$. Taking the area of contact to be $\mathcal{A}_{\mathrm{eff}} \approx 2\pi RD$, we find $\Delta T \approx (Z_S'' a_S^2 \omega/2\pi R\lambda)$. We take a thermal conductivity $\lambda \approx 0.1\ \mathrm{W\,m^{-1}\,K^{-1}}$, a yield shear dissipative impedance $Z_S'' \approx 10^3\ \mathrm{N/m}$ and a yield shear oscillation amplitude $a_S \approx 10$ nm. Eventually, we find a corresponding temperature increase $\Delta T \approx 6 \times 10^{-8}$ K which discards any thermal effect in the change of the interfacial structure's mechanical properties.

7. Effective area definition

Flow effective area.—The sphere oscillation induces a flow with an effective area of radius $\sqrt{2RD}$ and which is called the hydrodynamic probe radius [25]. Then the flow effective area reads $\mathcal{A}_{\mathrm{eff}} \approx \mathcal{A}_{\mathrm{hydro}} = 2\pi RD$.

Contact effective area.—The Hertz model enables us to estimate the effective area of contact over which the applied strain is distributed. For such a model, we consider that the interfacial solid indentation starts when we reach the frictional contact at $D = \lambda_S$. Then, the indentation depth reads $\delta = \lambda_S - D$, for $D < \lambda_S$. The model gives a circular contact of radius $c = \sqrt{2R\delta}$ and eventually a contact area $\mathcal{A}_{\mathrm{eff}} \approx \mathcal{A}_{\mathrm{Hertz}} = 2\pi R\delta$. We make use of the simple Hertz model because it is the one that requires fewer external parameters. A more developed model such as, for example, the Johnson, Kendall, and Roberts model taking into account adhesion forces, might be a better fit to completely describe the contact mechanics, but it would also require to input the adhesion work as an external parameter.

Limitations arise from the use of the abovementioned contact mechanics models to quantitatively compute physical quantities such as the load force as inelastic perturbations may arise and a quantitative Young modulus determination is needed.

[1] A. M. Smith, A. A. Lee, and S. Perkin, *The Electrostatic Screening Length in Concentrated Electrolytes Increases with Concentration*, J. Phys. Chem. Lett. **7**, 2157 (2016).

[2] M. A. Gebbie, A. M. Smith, H. A. Dobbs, A. A. Lee, G. G. Warr, X. Banquy, M. Valtiner, M. W. Rutland, J. N. Israelachvili, S. Perkin, and R. Atkin, *Long Range Electrostatic Forces in Ionic Liquids*, Chem. Commun. **53**, 1214 (2017).

[3] B. Rotenberg, O. Bernard, and J. P. Hansen, *Underscreening in Ionic Liquids: A First Principles Analysis*, J. Phys. Condens. Matter **30**, 054005 (2018).

[4] A. Maali and B. Bhushan, *Nanorheology and Boundary Slip in Confined Liquids Using Atomic Force Microscopy*, J. Phys. Condens. Matter **20**, 315201 (2008).

[5] S. Perkin, *Ionic Liquids in Confined Geometries*, Phys. Chem. Chem. Phys. **14**, 5052 (2012).

[6] S. Perkin, L. Crowhurst, H. Niedermeyer, T. Welton, A. M. Smith, and N. N. Gosvami, *Self-Assembly in the Electrical Double Layer of Ionic Liquids*, Chem. Commun. **47**, 6572 (2011).

[7] R. Futamura, T. Iiyama, Y. Takasaki, Y. Gogotsi, M. J. Biggs, M. Salanne, J. Ségalini, P. Simon, and K. Kaneko, *Partial Breaking of the Coulombic Ordering of Ionic Liquids Confined in Carbon Nanopores*, Nat. Mater. **16**, 1225 (2017).

[8] M. Galluzzi, S. Bovio, P. Milani, and A. Podestà, *Surface Confinement Induces the Formation of Solid-Like Insulating Ionic Liquid Nanostructures*, J. Phys. Chem. C **122**, 7934 (2018).

[9] L. A. Jurado and R. M. Espinosa-Marzal, *Insight into the Electrical Double Layer of an Ionic Liquid on Graphene*, Sci. Rep. **7**, 1 (2017).

[10] A. A. Lee and S. Perkin, *Ion-Image Interactions and Phase Transition at Electrolyte-Metal Interfaces*, J. Phys. Chem. Lett. **7**, 2753 (2016).

[11] N. Voeltzel, N. Fillot, P. Vergne, and L. Joly, *Orders of Magnitude Changes in the Friction of an Ionic Liquid on Carbonaceous Surfaces*, J. Phys. Chem. C **122**, 2145 (2018).

[12] H. Li, F. Endres, and R. Atkin, *Effect of Alkyl Chain Length and Anion Species on the Interfacial Nanostructure of Ionic Liquids at the Au(111) Ionic Liquid Interface as a Function of Potential*, Phys. Chem. Chem. Phys. **15**, 14624 (2013).

[13] J. Hoth, F. Hausen, M. H. Müser, and R. Bennewitz, *Force Microscopy of Layering and Friction in an Ionic Liquid*, J. Phys. Condens. Matter **26**, 284110 (2014).

[14] K. Tomita, M. Mizukami, S. Nakano, N. Ohta, N. Yagi, and K. Kurihara, *X-Ray Diffraction and Resonance Shear Measurement of Nano-Confined Ionic Liquids*, Phys. Chem. Chem. Phys. **20**, 13714 (2018).

[15] A. M. Smith, K. R. J. Lovelock, N. N. Gosvami, T. Welton, and S. Perkin, *Quantized Friction across Ionic Liquid Thin Films*, Phys. Chem. Chem. Phys. **15**, 15317 (2013).

[16] J. Comtet, A. Niguès, V. Kaiser, B. Coasne, L. Bocquet, and A. Siria, *Nanoscale Capillary Freezing of Ionic Liquids Confined between Metallic Interfaces and the Role of Electronic Screening*, Nat. Mater. **16**, 634 (2017).

[17] V. Kaiser, J. Comtet, A. Niguès, A. Siria, B. Coasne, and L. Bocquet, *Electrostatic Interactions between Ions near Thomas-Fermi Substrates and the Surface Energy of Ionic Crystals at Imperfect Metals*, Faraday Discuss. **199**, 129 (2017).

[18] R. Lhermerout, C. Diederichs, and S. Perkin, *Are Ionic Liquids Good Boundary Lubricants? A Molecular Perspective*, Lubricants **6**, 9 (2018).

[19] X. Gong and L. Li, *Nanometer-Thick Ionic Liquids as Boundary Lubricants*, Adv. Eng. Mater. **20**, 1700617 (2018).

[20] M. Armand, F. Endres, D. R. Macfarlane, H. Ohno, and B. Scrosati, *Ionic-Liquid Materials for the Electrochemical Challenges of the Future*, Nat. Mater. **8**, 621 (2009).

[21] L. Canale, A. Laborieux, A. Aroul Morgane, L. Jubin, J. Comtet, A. Lainé, L. Bocquet, A. Siria, and A. Niguès, *MicroMegascope*, Nanotechnology **29**, 355501 (2018).

[22] A. Lainé, L. Jubin, L. Canale, L. Bocquet, A. Siria, S. H. Donaldson, and A. Niguès, *MicroMegascope Based Dynamic Surface Force Apparatus*, Nanotechnology **30**, 195502 (2019).

[23] D. Tomida, A. Kumagai, K. Qiao, and C. Yokoyama, *Viscosity of [bmim] [PF_6] and [bmim] [BF_4] at High Pressure*, Int. J. Thermophys. **27**, 39 (2006).

[24] L. A. Jurado, H. Kim, A. Rossi, A. Arcifa, J. K. Schuh, N. D. Spencer, C. Leal, R. H. Ewoldt, and R. M. Espinosa-Marzal, *Effect of the Environmental Humidity on the Bulk, Interfacial and Nanoconfined Properties of an Ionic Liquid*, Phys. Chem. Chem. Phys. **18**, 22719 (2016).

[25] S. Leroy and E. Charlaix, *Hydrodynamic Interactions for the Measurement of Thin Film Elastic Properties*, J. Fluid Mech. **674**, 389 (2011).

[26] F. Endres, N. Borisenko, S. Z. El Abedin, R. Hayes, and R. Atkin, *The Interface Ionic Liquid(s)/Electrode(s): In situ STM and AFM Measurements*, Faraday Discuss. **154**, 221 (2012).

[27] T. Mason, J. Bibette, and D. Weitz, *Yielding and Flow of Monodisperse Emulsions*, J. Colloid Interface Sci. **179**, 439 (1996).

[28] C. Christopoulou, G. Petekidis, B. Erwin, M. Cloitre, and D. Vlassopoulos, *Ageing and Yield Behaviour in Model Soft Colloidal Glasses*, Phil. Trans. R. Soc. A **367**, 5051 (2009).

[29] O. Kraft, P. A. Gruber, R. Mönig, and D. Weygand, *Plasticity in Confined Dimensions*, Annu. Rev. Mater. Res. **40**, 293 (2010).

[30] M. Q. Jiang, G. Wilde, and L. H. Dai, *Origin of Stress Overshoot in Amorphous Solids*, Mech. Mater. **81**, 72 (2015).

[31] C. P. Fredlake, J. M. Crosthwaite, D. G. Hert, S. N. V. K. Aki, and J. F. Brennecke, *Thermophysical Properties of Imidazolium-Based Ionic Liquids*, J. Chem. Eng. Data **49**, 954 (2004).

[32] J. Nishida, J. P. Breen, B. Wu, and M. D. Fayer, *Extraordinary Slowing of Structural Dynamics in Thin Films of a Room Temperature Ionic Liquid*, ACS Cent. Sci. **4**, 1065 (2018).

[33] F. Borghi, P. Milani, and A. Podestà, *Solidlike Ordering of Imidazolium-Based Ionic Liquids at Rough Nanostructured Oxidized Silicon Surfaces*, Langmuir **35**, 11881 (2019).

[34] F. Varnik, L. Bocquet, and J. L. Barrat, *A Study of the Static Yield Stress in a Binary Lennard-Jones Glass*, J. Chem. Phys. **120**, 2788 (2004).

[35] L. A. Jurado, H. Kim, A. Arcifa, A. Rossi, C. Leal, N. D. Spencer, and R. M. Espinosa-Marzal, *Irreversible Structural Change of a Dry Ionic Liquid under Nanoconfinement*, Phys. Chem. Chem. Phys. **17**, 13613 (2015).

[36] N. N. Gosvami, J. A. Bares, F. Mangolini, A. R. Konicek, D. G. Yablon, and R. W. Carpick, *Mechanisms of Antiwear Tribofilm Growth Revealed In Situ by Single-Asperity Sliding Contacts*, Science **348**, 102 (2015).

[37] J. Sweeney, F. Hausen, R. Hayes, G. B. Webber, F. Endres, M. W. Rutland, R. Bennewitz, and R. Atkin, *Control of Nanoscale Friction on Gold in an Ionic Liquid by a Potential-Dependent Ionic Lubricant Layer*, Phys. Rev. Lett. **109**, 155502 (2012).

[38] C. Dold, T. Amann, and A. Kailer, *Influence of Electric Potentials on Friction of Sliding Contacts Lubricated by an Ionic Liquid*, Phys. Chem. Chem. Phys. **17**, 10339 (2015).

[39] O. Y. Fajardo, F. Bresme, A. A. Kornyshev, and M. Urbakh, *Electrotunable Lubricity with Ionic Liquid Nanoscale Films*, Sci. Rep. **5**, 7698 (2015).